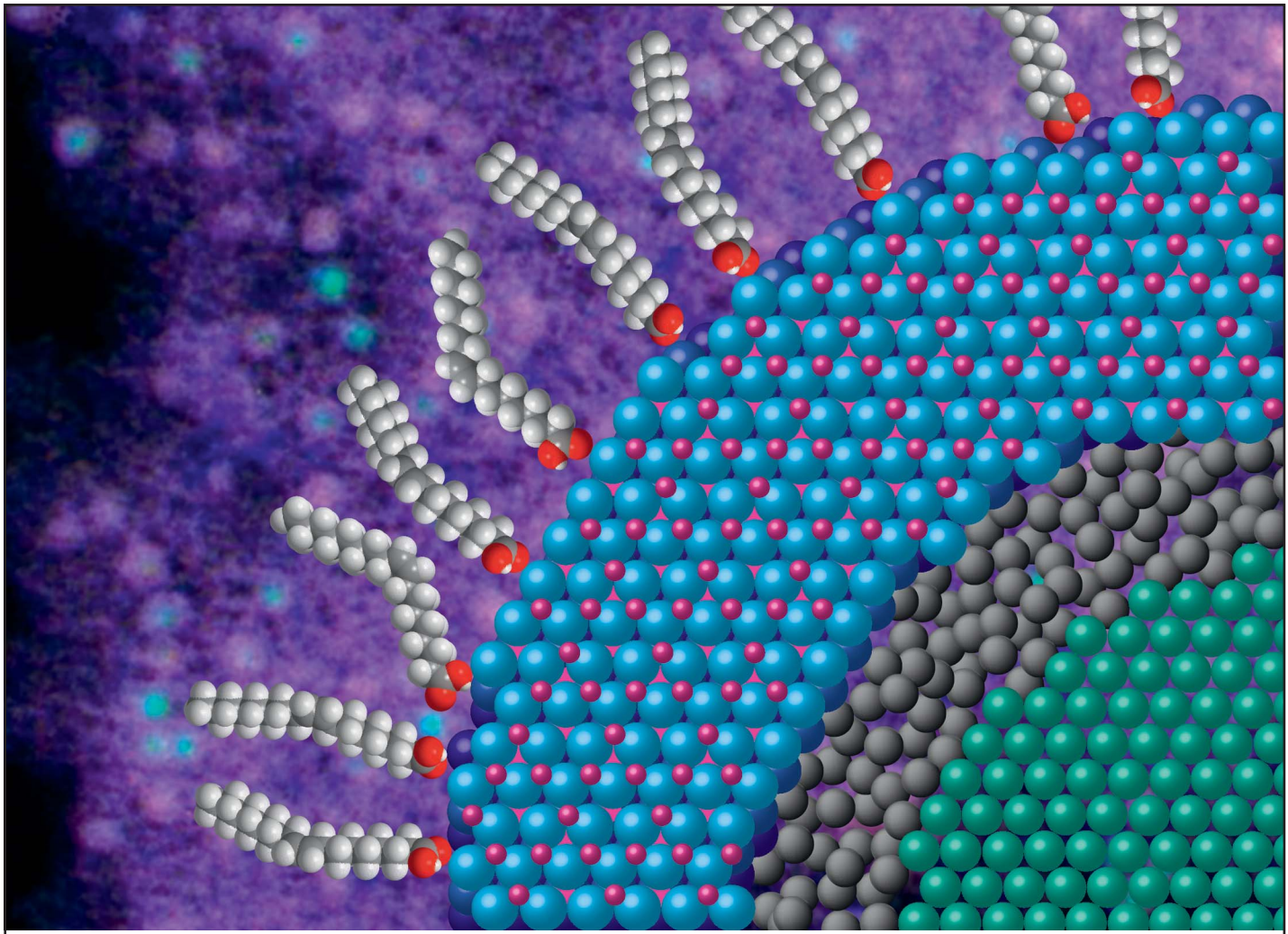

Collaborative research from the Universities of Cambridge and Oxford (UK), and the Instituto de Ciencia de Materiales de Sevilla (Spain) is funded in the framework of the Al-Nanofunc European project: "Advanced Laboratory for the Nano-analysis of Novel Functional Materials".

Title: Characterisation of Co@Fe_3O_4 core@shell nanoparticles using advanced electron microscopy

Core@shell nanoparticles were formed from the sequential decomposition of Co and Fe carbonyls, with organic capping agents present. Using statistically refined EFTEM and a calibrated EELS analysis, the phases of the core and shell of the nanoparticles were determined using the fine structure of the energy loss peaks of cobalt and iron. Additionally the presence of a carbonaceous layer of capping ligand residues separating the core and shell of the particles has been identified, shedding light on the possible mechanisms of particle formation and suggesting potential new routes to the synthesis of core@shell particles.

As featured in:

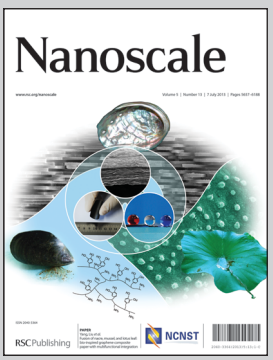

See Lozano-Perez, Fernández and Wheatley *et al.*, *Nanoscale*, 2013, **5**, 5765.

RSC Publishing

www.rsc.org/nanoscale

Registered Charity Number 207890

Nanoscale

RSC Publishing

PAPER

View Article Online
View Journal | View Issue

Cite this: *Nanoscale*, 2013, **5**, 5765

Characterisation of Co@Fe_3O_4 core@shell nanoparticles using advanced electron microscopy†

Benjamin R. Knappett,[a] Pavel Abdulkin,[a] Emilie Ringe,[b] David A. Jefferson,[a] Sergio Lozano-Perez,*[c] T. Cristina Rojas,[d] Asunción Fernández*[d] and Andrew E. H. Wheatley*[a]

Received 23rd November 2012
Accepted 17th February 2013

DOI: 10.1039/c3nr33789h

www.rsc.org/nanoscale

Cobalt nanoparticles were synthesised *via* the thermal decomposition of $Co_2(CO)_8$ and were coated in iron oxide using $Fe(CO)_5$. While previous work focused on the subsequent thermal alloying of these nanoparticles, this study fully elucidates their composition and core@shell structure. State-of-the-art electron microscopy and statistical data processing enabled chemical mapping of individual particles through the acquisition of energy-filtered transmission electron microscopy (EFTEM) images and detailed electron energy loss spectroscopy (EELS) analysis. Multivariate statistical analysis (MSA) has been used to greatly improve the quality of elemental mapping data from core@shell nanoparticles. Results from a combination of spatially resolved microanalysis reveal the shell as Fe_3O_4 and show that the core is composed of oxidatively stable metallic Co. For the first time, a region of lower atom density between the particle core and shell has been observed and identified as a trapped carbon residue attributable to the organic capping agents present in the initial Co nanoparticle synthesis.

Introduction

In recent years there has been significant interest in the synthesis of bimetallic or metal oxide nanoparticles (NPs) with a core@shell structure,[1–4] as they have been suggested for a number of applications such as magnetic separation,[5–7] catalysis,[8,9] targeted drug delivery,[10] and magnetic hyperthermia.[11–13] Central to these applications is the possibility of synthesising magnetic particles coated with a functional layer.[14,15] For instance, Lee *et al.* have shown that Ni@NiO NPs can be used, due to their superparamagnetic Ni cores, for the magnetic separation of specific histidine-tagged fluorescent proteins.[5] Similarly, Jun *et al.* synthesised Co@Pt NPs which function as magnetically separable hydrogenation catalysts.[15] This approach minimizes the amount of Pt needed by replacing the core of the particle with an inexpensive alternative, but most importantly has the advantage of lending magnetism to the catalytic particles.

Core@shell structures are often proposed in the catalysis literature, albeit evidence of successful synthesis is commonly based on bulk analysis techniques or on the increase in mean size between the pre-formed seed (core) NPs and the coated product. Whilst such results clearly indicate a change in the nature of the sample, they typically offer limited evidence regarding the structure and composition of a core@shell NP. Moreover, bulk methods can rarely differentiate between coating, heat-induced coalescence and alloying.[16] Powder X-ray diffraction (PXRD), a prevalent bulk technique, can provide some information about the average crystallite size and composition.[17] However, it remains difficult to extract NP size due to their polycrystallinity and the strong background caused by capping ligands.[18] The applicability of PXRD to these systems is also restricted by the limited spatial and structural information it provides; indeed, it remains difficult to differentiate between various NP structures (Fig. 1) without sophisticated modelling of the fine structure of the pattern,[19] which is often blurred by broadening.[20]

A consequence of the limitations of X-ray diffraction and other bulk characterisation techniques is that in order to identify the true structure of individual particles one must rely on more sophisticated approaches such as spatially resolved micro-analytical methods. Transmission electron microscopy (TEM) provides such a spatially resolved analysis platform ideally suited to the characterisation of multi-layered nanostructures. Bright field TEM and high resolution TEM (HRTEM) can be used to discern different compositions based on lattice fringes and contrast variations.[21,22] Dark field imaging

[a]*Department of Chemistry, University of Cambridge, Lensfield Road, Cambridge, CB2 1EW, UK. E-mail: aehw2@cam.ac.uk*

[b]*Department of Materials Science and Metallurgy, University of Cambridge, Pembroke Street, Cambridge, CB2 3QZ, UK*

[c]*Department of Materials, University of Oxford, Parks Road, Oxford, OX1 3PH, UK. E-mail: sergio.lozano-perez@materials.ox.ac.uk*

[d]*Instituto de Ciencia de Materiales de Sevilla (ICMS), CSIC–Univ. Sevilla, Américo Vespucio 49, Isla de la Cartuja, 41092-Sevilla, Spain. E-mail: asuncion@icmse.csic.es*

† Electronic supplementary information (ESI) available: Further HRTEM images, EDS, EELS and EDS line scans, EFTEM and eigenvectors for MSA analysis. See DOI: 10.1039/c3nr33789h

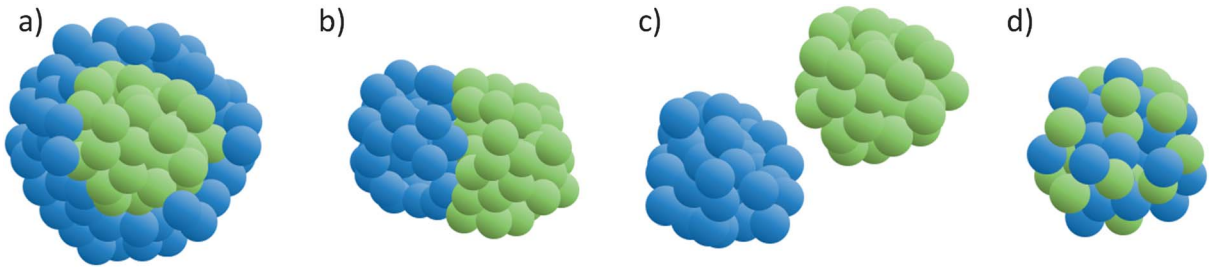

Fig. 1 Diagrammatic representations of bimetallic 1D nano-materials with (a) core@shell; (b) fused; (c) segregated and (d) random alloy structures.

techniques such as high angle annular dark field (HAADF) are also extremely instructive in this latter respect, since image formation now occurs using predominantly Rutherford scattered electrons, rather than the predominantly Bragg scattered electrons of bright field imaging.[23,24] The much greater susceptibility of Rutherford scattered electrons to differences in atomic number, Z, of the scattering atoms has resulted in dark field scanning TEM often being referred to as Z-contrast TEM.[25] Scanning TEM (STEM) can thus be used to create dark field images in which the contrast ratios are proportional to the Z number of atoms in the material generating the signal.[23] Crucially for the elucidation of single particle composition, STEM also allows for spatially resolved energy dispersive spectroscopy (EDS) and electron energy loss spectroscopy (EELS)[26–29] using a sub-nanometre probe size, providing elemental line scans or maps of individual particles.[30]

Another form of microanalysis, energy-filtered TEM (EFTEM), involves the selection of electrons with a particular energy loss to form images. By selecting the energy corresponding to core losses for particular elements, images can be created almost exclusively with electrons scattered by that particular element. By taking multiple images corresponding to signals from different elements, composite maps can be created revealing the prevalence of multiple elements. Langlois *et al.* recently used this technique to analyse Cu@Ag core@shell particles.[31]

Generally the resolution limit of EFTEM is approximately 1 nm,[32] although in the case of NPs, it is greatly compromised by the low signal (and therefore high noise) in the elemental images. To circumvent this major drawback, we have implemented a mathematical algorithm based on Multivariate Statistical Analysis (MSA) to refine analytical data (EDS and EELS line profiles as well as EFTEM images) by separating any meaningful information from statistical noise. This allows for data reconstruction with a significantly reduced noise signal.[33] Used in conjunction, these experimental and data analysis techniques allow for a thorough characterisation of nanosized particles.

The current study explores the oxidative stability of cobalt on the nanoscale as well as the composition of its iron oxide outer shell. Co NPs are not oxidatively stable with respect to the antiferromagnetic CoO phase, so if magnetism is to be retained they require protection, either by organic material[34] or by a more permanent layer of inorganic material such as iron oxide. A Co/Fe system was previously synthesised by Sun *et al.*, however their interest focussed on the magnetic properties of the particles after thermal annealing, which resulted in the formation of a controlled, stoichiometric CoFe alloy.[1,35] The current work explores in detail the composition and structure of the core@shell particles attained prior to annealing by using a combination of cutting-edge electron microscopy, microanalysis, and statistical analysis techniques.

Experimental techniques

Synthesis of cobalt cores

Co seed NPs were prepared following a modified literature synthesis.[36] 2 mmol of $Co_2(CO)_8$ (0.68 g, >90% moistened with hexane, Sigma Aldrich) was dissolved in 5 ml of 1,2-dichlorobenzene (DCB, 99%, Sigma Aldrich) and injected into a degassed solution of 2.0 mmol oleic acid (0.65 ml, 99%, Sigma Aldrich) and 2.0 mmol triphenylphosphine (0.52 g, 99%, Sigma Aldrich), also in DCB (40 ml) under a blanket of nitrogen at 60 °C. After initial effervescence had subsided, the solution was heated to 185 °C for 30 minutes, and then left to cool.

Iron coating of cobalt cores

The iron coating procedure was based on a modified literature method of Sun *et al.*[35] The Co seeds in DCB were heated to 120 °C and $Fe(CO)_5$ (0.18 mol, 0.9 ml) was added. After 30 minutes, the temperature was increased to 180 °C at a rate of 2–3 °C min^{-1}, and was then kept at this temperature for an additional 30 minutes. The temperature was then increased to 250 °C for 15 minutes, before the sample was allowed to cool to room temperature. The resulting NPs were purified by precipitation in excess ethanol, followed by re-dispersion in the minimum volume of hexane (4–5 ml) and by a second precipitation. The particles were finally dispersed in hexane (10 ml).

Characterisation

Samples were prepared by drop-coating hexane suspensions onto holey carbon coated Cu grids (Agar Scientific, 300 mesh). An image aberration corrected FEI Titan 80-300 with an operating voltage of 300 keV and a point resolution of 0.08 nm in TEM mode was used to obtain the data presented in Fig. 2–5. STEM was performed using a HAADF detector with a nominal spot size of 0.14 nm. For spectroscopy, a nominal spot size of ~0.5 nm was used in STEM mode with a Gatan Tridiem image filter for EELS and an EDAX S-UTW EDS detector. The sample

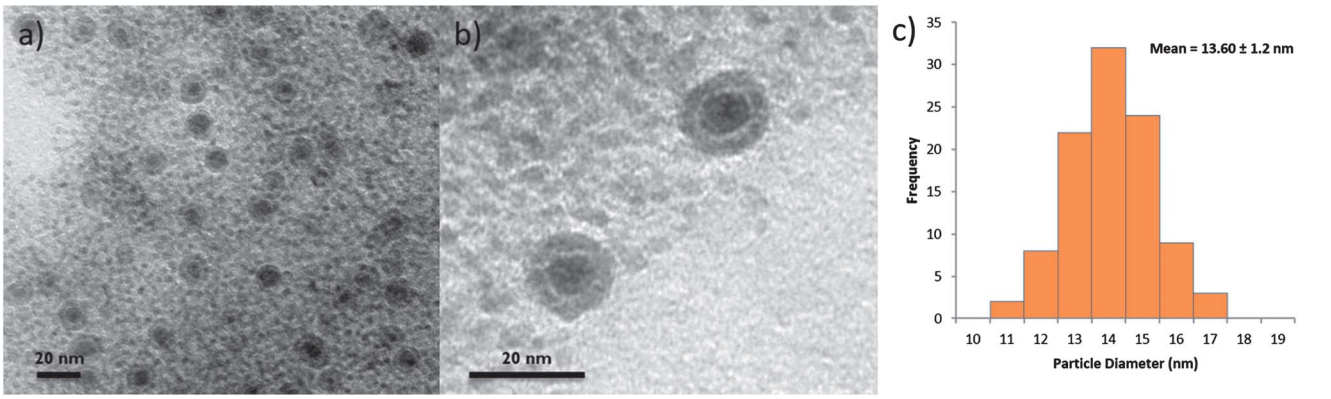

Fig. 2 (a and b) TEM images in bright field imaging mode of monodisperse 14 nm Co@Fe_3O_4 NPs, along with (c) the particle size distribution of the core@shell particles ($N = 100$).

was subsequently imaged using a field emission gun (FEG) JEOL JEM-3000F TEM at an operating voltage of 297 keV equipped with a Gatan image filter (GIF) 2002 for EELS and an Oxford Instruments Si/Li EDS detector with an Inca analytical system. The data from Fig. 6–8 and 10 were acquired using this microscope. EFTEM images were acquired between 650 and 850 eV, in steps of 10 eV and with a slit width of 10 eV. For all images, convergence and collection half-angles of 3 and 20 mrad were used, respectively. In order to minimise beam damage, each pixel was sampled for 1 s, during which time the ~1 Å probe was oscillated within the 1 nm target, so as to minimise the amount of time the beam spent stationary on the sample. Each line was scanned 20 times, to improve the signal-to-noise ratio sufficiently for the data to be reliable.

An FEI Tecnai F20 with a 200 keV FEG was used in STEM mode to acquire the experimental EELS data from Fig. 9 and 11. This microscope was equipped with a GIF 200 and a Fischione model 3000 HAADF detector for high-resolution *Z*-contrast imaging. The Si_3N_4 grids used with this microscope had a 10 nm thick Si_3N_4 membrane (supplied by TEMWindows).

The EELS of reference materials are displayed in Fig. 9 and were measured with a PEELS spectrometer (Gatan mod766-2K) coupled to a Philips CM200 TEM microscope. All the spectra were corrected for dark current and channel-to-channel gain variation. A low-loss spectrum was also recorded with each edge in the same illuminated area and using the same experimental conditions. After subtraction of the background with a standard power law function, the spectra were de-convoluted for plural scattering with the Fourier-ratio method. All these treatments were performed within the EL/P program (Gatan).

Results and discussion

Crystallographic analysis

Decomposition of $Fe(CO)_5$ in the presence of oleic acid-capped Co NPs yielded two distinct types of particle (Fig. 2): small (~2 nm diameter) uniform NPs as well as larger core@shell structures. The latter have a monodisperse,[39] mono-modal size distribution with a mean particle size of 13.6 nm and a standard deviation of 1.2 nm (9%, $N = 100$; see Fig. 2). These core@shell NPs are approximately spherical with small variations in aspect ratio and surface roughness, likely due to multiple nucleation sites leading to growth of a polycrystalline shell. This can be seen in Fig. 3b as a petal-like arrangement in the shell.

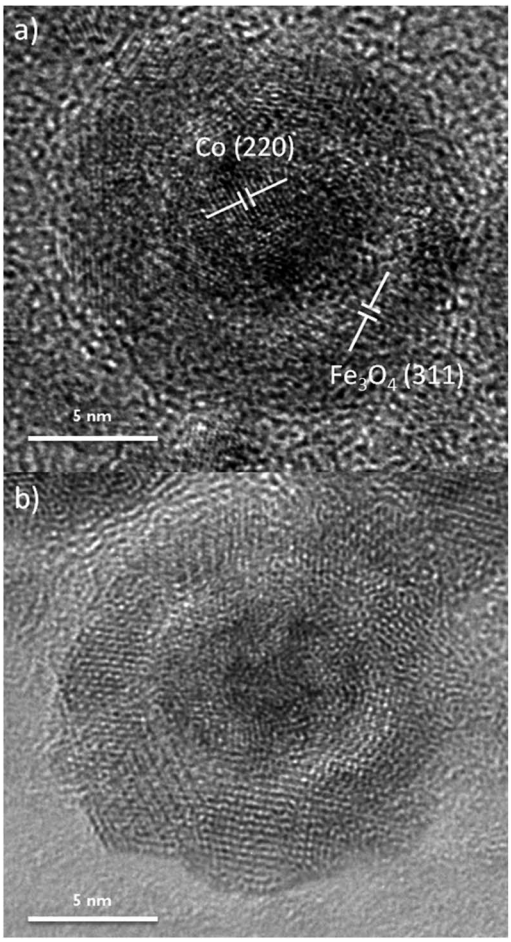

Fig. 3 HRTEM images showing fringes in the core and shell of a particle. The image in (a) highlights the 2.16 Å *d*-spacing of the (220) reflection of metallic Co in the core[37] and the 2.51 Å *d*-spacing of the (311) reflection of Fe_3O_4 in the shell,[38] whilst that in (b) shows the 'petal-like' structure of the shell caused by multiple nucleation sites. Additional HRTEM images can be found in the ESI.†

The HRTEM images clearly show the presence of a lower contrast shell surrounding a darker core. Lattice fringes are present in both regions, suggesting the existence of a crystalline core@shell structure as previously pointed out by Sun *et al.*,[35] rather than a coating of solely organic residues from the synthesis. Fringes of 2.16 Å and 2.51 Å were observed in the core and shell, respectively, corresponding well to the Co (220) and the Fe_3O_4 (311) lattice spacings (Fig. 3). A large number of ~2 nm particles of light contrast with lattice fringes consistent with Fe_3O_4 (see ESI†) are also present. Their formation is attributed to the use of excess $Fe(CO)_5$, yielding discrete iron oxide particles in addition to shells. The larger core@shell particles are readily distinguishable from these particles (Fig. 2b). No uncoated cores were observed, suggesting a successful and complete coating was achieved.

Interestingly, high magnification images also show a lighter region between the core and shell of individual NPs (Fig. 3a and b). This region is consistently devoid of fringes, suggesting a non-crystalline substance potentially derived from the surfactants used to stabilise the Co seeds. The outer iron oxide shell has evidently formed around this layer, encapsulating it within the particle. The novelty of this observation prompted us to further analyse this layer with elemental analysis techniques (*vide infra*).

In addition to real-space fringe spacing analysis, we acquired selected area electron diffraction (SAED) from a large region containing NPs, an example of which is shown in Fig. 4. The rings present in the pattern reveal the lattice spacing in the polycrystalline sample; the experimental values of 3.01, 2.56, 2.11, 1.71 and 1.51 Å correspond with the Fe_3O_4 (220), Fe_3O_4 (311), Fe_3O_4 (400)/Co (220), Fe_3O_4 (511), and Fe_3O_4 (440) reflections. The spacing expected for Co (220) is 2.16 Å, thus the signal for this is likely obscured by the (400) reflection from the excess of Fe_3O_4 present. Similarly, the fast Fourier transform (FFT) of images of individual NPs such as the one in Fig. 4 (which match the SAED in diameter to within 4% error) show prominent reflections for lattice spacings of 2.54, 2.10 and 1.47 Å, corresponding to the Fe_3O_4 (311), Co (200)/Fe_3O_4 (400), and Fe_3O_4 (440) spacings. Based on this analysis, it can be concluded that the Co is present in a metallic, non-oxidized form. However, while the lattice fringe analysis rules out the presence of α-Fe_2O_3 on the basis of its different lattice parameters, HRTEM alone is not sufficient to fully distinguish between the two spinel structures of iron oxide (Fe_3O_4 and γ-Fe_2O_3). This distinction will be discussed later, supported by EELS data.

Core@Shell structure

By imaging with the electrons that have an energy loss corresponding to core losses of particular elements using EFTEM, one can obtain elemental information with high spatial resolution. A series of EFTEM images of the core@shell NPs were recorded using a 10 eV slit width. Images before and after the Co $L_{2,3}$, iron $L_{2,3}$ and oxygen K edges were acquired and elemental maps were created using a 3-window technique. This gave a preliminary indication of the particle structure and elemental composition. In Fig. 5a, a TEM bright field image is presented alongside EFTEM Co $L_{2,3}$ and Fe $L_{2,3}$ maps (Fig. 5b and c). The high concentration of Co in the cores and the tendency for iron and oxygen accretion to form a shell are clearly visible. Furthermore, the 2 nm particles appear to be composed of oxygen and iron, with lattice fringe analysis and EELS data (see ESI†) obtained for these small particles suggesting the Fe_3O_4 phase. Additional EFTEM series on larger areas were acquired, covering the Fe and Co $L_{2,3}$ edges, and MSA was applied to yield

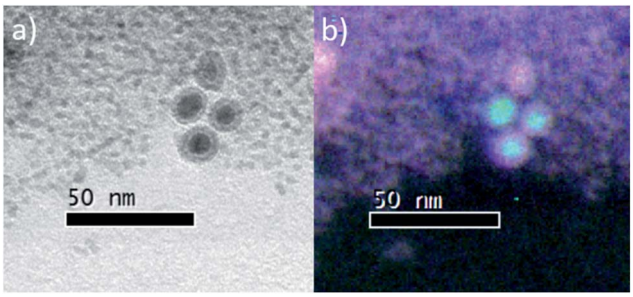

Fig. 5 EFTEM images of Co@Fe_3O_4 core@shell particles. (a) Bright field TEM image and (b) an overlay of Co (green), Fe (pink) and O (blue) compositional maps. An EDS map showing similar evidence can be found in the ESI.†

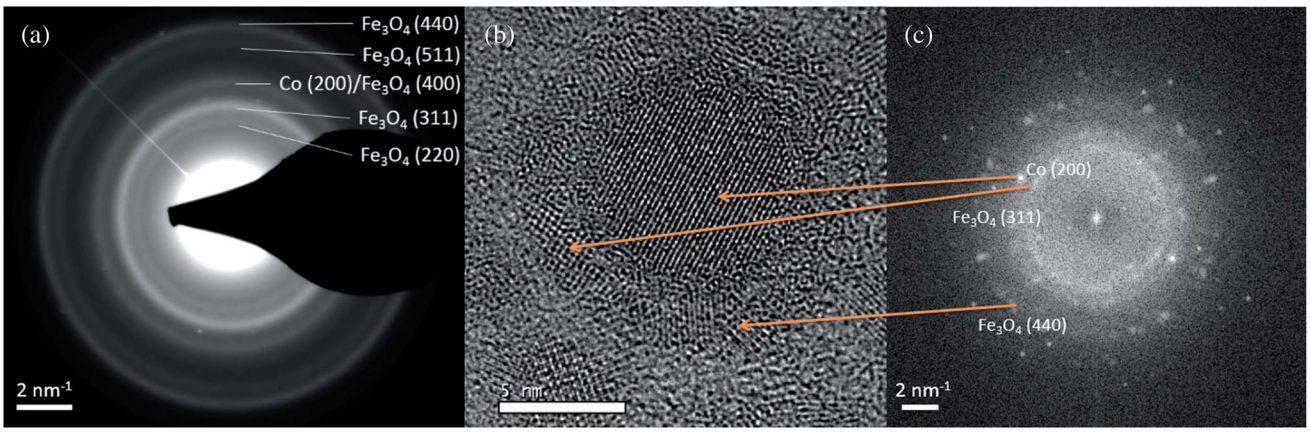

Fig. 4 (a) SAED image of a sample region containing multiple core@shell NPs, shown alongside a TEM image of an individual NP (b) with corresponding FFT (c).

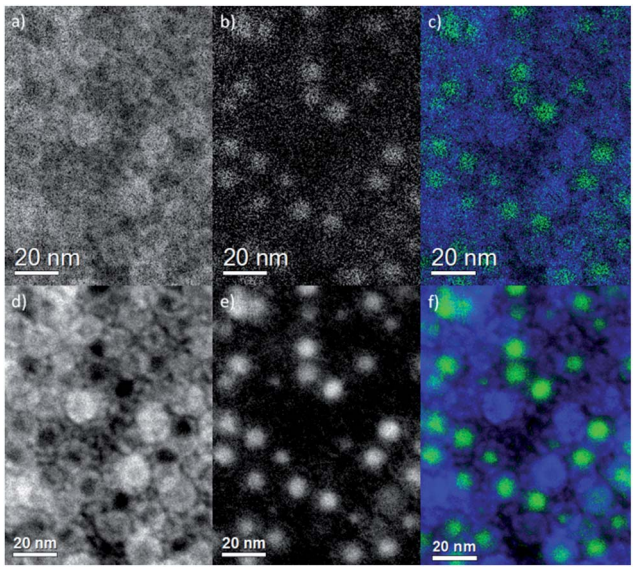

Fig. 6 EFTEM images of Co@Fe_3O_4 core@shell particles, both before (a–c) and after (d–f) MSA. (a and d) EFTEM Fe $L_{2,3}$ map; (b and e) EFTEM Co $L_{2,3}$ map; (c and f) an overlay of Co and Fe maps, with Co in green and Fe in blue.

the clear images of the Co cores and Fe shells presented in Fig. 6; a major improvement in the quality of the data after MSA can be observed. It appears evident from such analysis that the location of Co perfectly matches that of the darker contrast cores in bright field images.

Another way to obtain spatially resolved chemical information about complex nanostructures is by obtaining a full energy loss spectrum from a series of points across the particle in a STEM configuration, which allows the extraction of linear compositional variation. Note that in such a configuration, images are obtained from a HAADF detector, which provides density-based contrast, the cores appearing bright due to their higher scattering probability. STEM-EELS is in fact ideal for observing Fe, Co and O as their core losses lie within 500 eV of one another, allowing for high resolution simultaneous acquisition. As can be seen in Fig. 7, the line profile for Co $L_{2,3}$ shows a strong peak corresponding to the position of the bright particle core, whilst the spectra on either side of the core are dominated by Fe $L_{2,3}$ and O K edges. Care was taken to minimize beam damage (see experimental section); images showing only minor damage to the NP after the scan are reported in Fig. 7 and 8.

To confirm and further investigate the elemental distribution in individual NPs, STEM-based EDS was used to obtain line scans (an example of which is presented in Fig. 8) as well as area scans (reported in the ESI†). The presence of Co, Fe, and O was confirmed. Due to the minute amount of material illuminated by the probe (and resulting low X-ray emission probability[40]) the EDS signal intensity was very low; whilst the signal could be improved by increasing the beam current or acquisition time, either would risk damaging the sample. Reduced signal strength was tolerated in order to minimise damage, and was

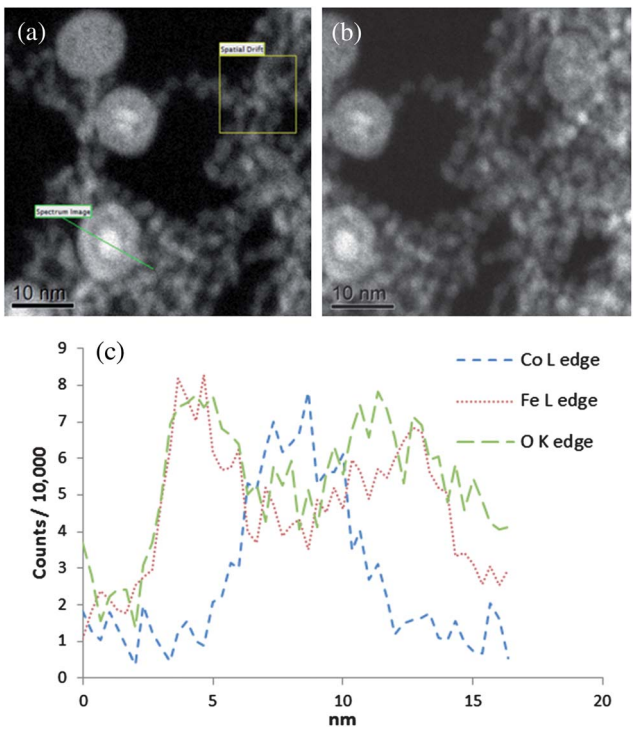

Fig. 7 An EELS line scan of a core@shell particle. (a) STEM HAADF image showing the square region (yellow box) selected for spatial drift correction, and position of the line scan (green line); (b) acquisition region post-scan; and (c) graph showing the EELS signal intensity after MSA for Co, Fe and O across the diameter of the particle.

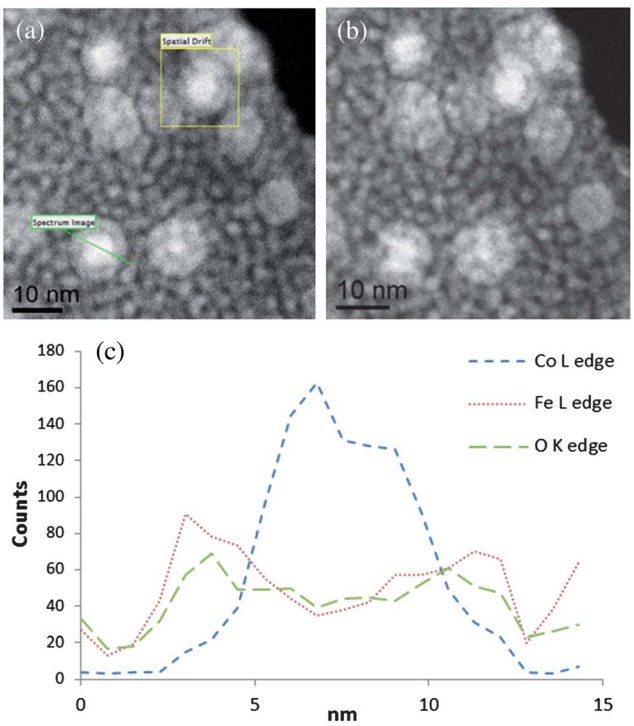

Fig. 8 An EDS line scan of a core@shell particle. (a) STEM HAADF image showing the region selected for drift correction (yellow box), and position of the line scan (green line); (b) the acquisition region post-scan, showing that some minor damage has occurred; and (c) graph showing the EDS signal intensity for Co, Fe and O across the diameter of the particle.

compensated for by the final MSA processing, allowing for a more meaningful interpretation of the data. Clearly, as can be seen in Fig. 8, minimal damage was inflicted, while conclusive results could be extracted. Indeed, the EDS line scan data clearly confirms that the centre of the NP contains mostly Co surrounded by a shell of Fe and O. While EDS is not as sensitive to O as EELS, it provides strong concurrent evidence for the NP structure.

Iron and cobalt oxidation state

Knowledge of the oxidation state of both Fe and Co is critical for a better understanding of this NP system, especially given the magnetic properties of metallic Co. The relative closeness in energy of the Fe L_3 edge for different phases[41] and the large energy shift between oxidized and metallic Co (>4.5 eV (ref. 42)) allowed us to use the energy difference between the L_3 edges of Fe and Co to confirm the presence of metallic Co only. Indeed, EELS point scans of the central region of 39 NPs revealed a stable difference between the Co and Fe L_3 edge of 71.0(3) eV (standard deviation on the last digit in parenthesis), perfectly matching the expected 71.3 eV shift between Fe_3O_4 and metallic Co.[41] Note that all shifts between oxidized Co and any of the iron oxide phases considered would be above 74 eV, a value statistically different to that obtained experimentally.

Regarding the iron oxide, the diffraction and lattice fringe analysis discussed above suggested the absence of α-Fe_2O_3, but could not clearly differentiate between the spinel structures of Fe_3O_4 and γ-Fe_2O_3. In this respect, EELS coupled with statistical analysis can provide additional information. Firstly, EELS analysis of 95 single particles further rules out the presence of α-Fe_2O_3. Indeed, as can be seen in Fig. 9, the Fe L_3–L_2 shift of the α-phase is much larger (15.8 eV) than the 12.5(3) eV observed. This experimental L_3–L_2 energy difference also suggests the presence of Fe_3O_4 (12.7 eV) rather than γ-Fe_2O_3 (12.9 eV).

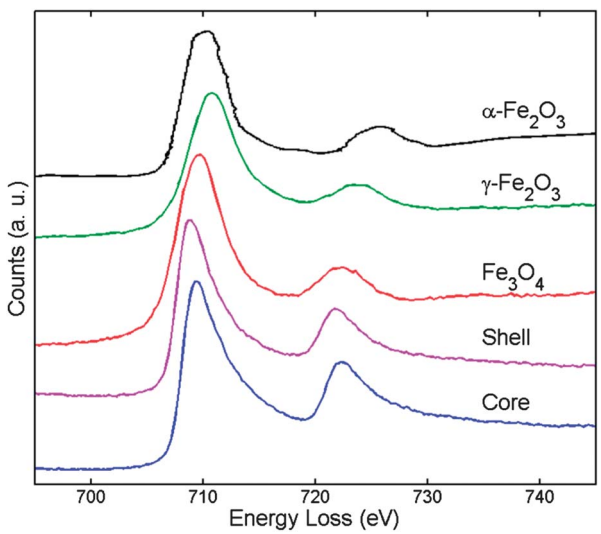

Fig. 9 EELS of the iron $L_{2,3}$ edge, averaged over 95 point scans of the core and shell regions of the NPs, compared to the EELS of reference materials for each of Fe_3O_4, γ-Fe_2O_3 and α-Fe_2O_3 (99%, Sigma).

Furthermore, the Fe–Co difference of 71.0(3) eV can only be attributed to the Fe_3O_4 phase, as the expected value for γ-Fe_2O_3 (70.2) is significantly different.

Having confirmed the composition of both core (Co) and shell (Fe_3O_4), we became interested in the oxidative stability of the NPs. Indeed, it is desirable for applications that the Co core remains metallic and does not oxidize to the antiferromagnetic CoO phase. To study oxidation (and the presence of carbon between the layers as will be seen later), NPs deposited on thin Si_3N_4 membranes were submitted to the strongly oxidizing conditions of an oxygen–argon plasma for 15 minutes and analysed with EELS. No change in composition of either the core or the shell was observed from the spectra of 41 NPs; suggesting that the iron oxide coating effectively stabilises the Co core with respect to oxidation.

Presence of a trapped carbon layer

High resolution images of the core@shell NPs commonly displayed a small amorphous layer of unknown composition between the core and shell. As a first attempt to elucidate its nature, a typical particle, displaying the bright central contrast of a core–shell structure in the HAADF image, was scanned across with STEM-EELS and a profile containing information about Fe, O, and C content was obtained (Fig. 10). Signal from Co could not, at this time, be simultaneously recorded due to instrumental limitations.

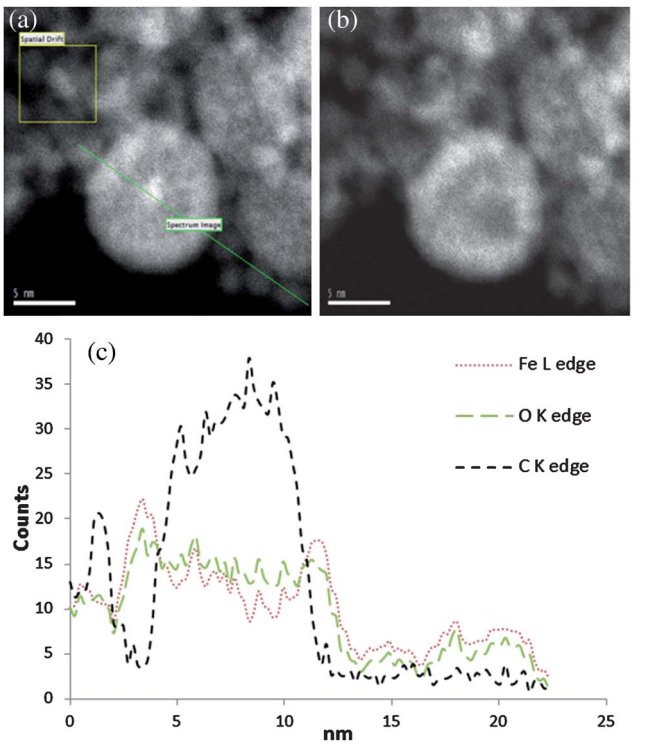

Fig. 10 An EELS line scan of a core@shell particle. (a) STEM HAADF image showing the square region selected for spatial drift correction, and position of the line scan; (b) acquisition region post-scan, with some particle damage observable; and (c) graph showing the EELS signal intensity after MSA for Fe, O and C across the diameter of the particle.

Fig. 10 reveals the presence of carbon within the NP, with a strong signal through the core region. The high carbon region is also clearly contained between the Fe and O maxima attributable to the iron oxide shell, within which it drops sharply to background levels. This scan shows for the first time evidence of a carbon based layer between the core and shell of Co@Fe_3O_4 particles. It should be noted that this line scan was carried out using a carbon-based grid, however the scan was intentionally positioned to span a region several nanometres beyond boundaries of the core@shell NP, showing the intensity of the background signal generated by the carbon film to be an order of magnitude lower than that observed in the particle core.

To further study the presence of carbon within the shell, particles were deposited on a carbon-free Si_3N_4 membrane. STEM-EELS analysis revealed the presence of carbon in the core@shell NPs. To rule out the possibility of carbon contamination at the surface of the Fe_3O_4 shell and provide strong evidence of its presence *within* the particle, a sample supported on a Si_3N_4 membrane was plasma-cleaned in an argon–oxygen mixture for 15 minutes. Plasma cleaning indeed removes any carbonaceous material that may be present on the surface of the NPs. STEM-EELS point scans of over 50 NPs revealed the presence of carbon at the interface between Co and Fe_3O_4, while no carbon signal could be detected on the Si_3N_4 membrane (Fig. 11). This information, in addition to the line scan presented in Fig. 10, provides clear evidence for the presence of a trapped carbon-based layer within the core@shell NPs, a novel finding made possible by the use of advanced TEM-based microanalysis. The presence of this layer could favour the growth of Fe_3O_4 on Co by lowering the epitaxial constraints at the interface, effectively acting as a buffer layer; a concept which could give rise to new synthetic approaches.

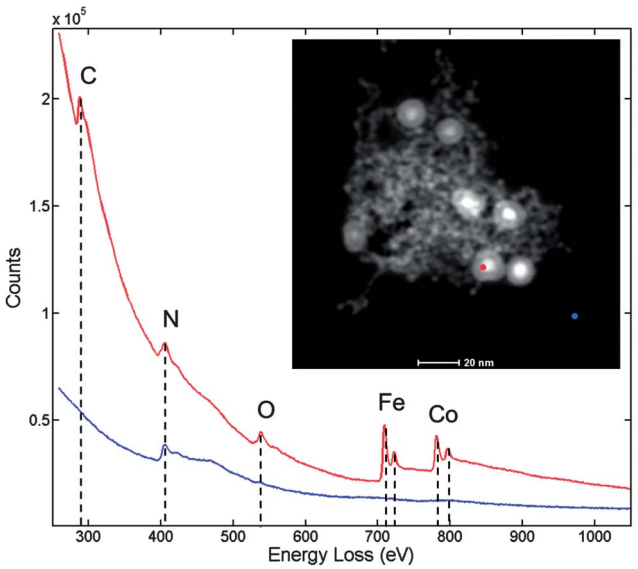

Fig. 11 EELS point spectra (from a plasma cleaned sample) of the Si_3N_4 thin film coating the microscope grid (blue spot and line) and of the interface of the core and shell of a core@shell particle (red). It can be clearly seen that carbon is present within the particle despite plasma cleaning.

Conclusions

Using a variety of state-of-the-art microanalysis techniques combined with statistics and MSA, the detailed chemical composition of Co@Fe_3O_4 core@shell NPs has been revealed. Composition maps were obtained, and the phase and oxidation states of the core and shell components were identified. Elemental analysis from line scans acquired with STEM-EDS and STEM-EELS further elucidated the details of particle structure. Minimal beam damage was inflicted on the particles by carefully controlling the beam current and scan repetition and rate. The resolution of mapping techniques was substantially enhanced using MSA, eliminating much of the noise in the spectra. The difference in *Z* contrast and lattice fringes between the core and shell indicate a core@shell structure; rigorous microanalysis with EFTEM, STEM-EDS and STEM-EELS verified the coating of metallic Co seeds by a polycrystalline Fe_3O_4 shell.

Interestingly, the oxide shell appears to be separated from the core by a non-crystalline carbon layer, which we propose to be composed of trapped oleic acid residues present from the initial synthesis of the seed particles. This is identifiable by the difference in contrast in HRTEM images, and is well evidenced by the detection of carbon within the particles by EELS line scans and also EELS point spectra of the particles on a plasma cleaned, carbon-free support membrane.

Analysis of a large number of NPs after a period of months showed that the particle cores had not oxidised, and even remained as metallic Co after being subjected to an oxygen plasma. It can therefore be concluded that the Fe_3O_4 provides a suitable barrier to core oxidation, allowing the particles to retain their magnetic properties during storage and potential catalytic applications.

Having demonstrated the ability of the combination of techniques described here to probe individual NP structure and stability in detail, unravelling novel information about their composition, we now seek to characterise further examples of core@shell particles.

Acknowledgements

This work was partly carried out with the support of the Karlsruhe Nano Micro Facility (KNMF, http://www.kit.edu/knmf), a Helmholtz Research Infrastructure at Karlsruhe Institute of Technology (KIT, http://www.kit.edu) and the authors wish to thank Drs Christian Kübel and Di Wang for assistance with data acquisition. They also gratefully acknowledge financial support from The Junta de Andalucía (FEDER PE2009-FQM-4554, TEP-217) and EU FP7 AL-NANOFUNC project (CT-REGPOT2011-1-285895). B. R. K. thanks the UK EPSRC, The University of Cambridge and Downing College for grants. E. R. acknowledges support from the Royal Society in the form of a Newton International Fellowship.

Notes and references

1 S. Peng, J. Xie and S. Sun, *J. Solid State Chem.*, 2008, **181**, 1560–1564.

2 J. Gallo, I. García, D. Padro, B. Arnáiz and S. Penadés, *J. Mater. Chem.*, 2010, **20**, 10010.
3 W.-R. Lee, M. G. Kim, J.-R. Choi, J.-I. Park, S. J. Ko, S. J. Oh and J. Cheon, *J. Am. Chem. Soc.*, 2005, **127**, 16090–16097.
4 G. Schmid, H. West, J.-O. Malm, J.-O. Bovin and C. Grenthe, *Chem.–Eur. J.*, 1996, **2**, 1099.
5 I. S. Lee, N. Lee, J. Park, B. H. Kim, Y.-W. Yi, T. Kim, T. K. Kim, I. H. Lee, S. R. Paik and T. Hyeon, *J. Am. Chem. Soc.*, 2006, **128**, 10658–10659.
6 H.-Y. Park, M. J. Schadt, L. Wang, I.-I. S. Lim, P. N. Njoki, S. H. Kim, M.-Y. Jang, J. Luo and C.-J. Zhong, *Langmuir*, 2007, **23**, 9050–9056.
7 Y.-R. Cui, C. Hong, Y.-L. Zhou, Y. Li, X.-M. Gao and X.-X. Zhang, *Talanta*, 2011, **85**, 1246–1252.
8 N. Toshima, *Pure Appl. Chem.*, 2000, **72**, 317–325.
9 D. Bai, Q. Wang, Y. Song, B. Li and H. Jing, *Catal. Commun.*, 2011, **12**, 684–688.
10 J. Dobson, *Drug Dev. Res.*, 2006, **67**, 55–60.
11 Q. A. Pankhurst, J. Connolly, S. K. Jones and J. Dobson, *J. Phys. D: Appl. Phys.*, 2003, **36**, R167–R181.
12 P. Gangopadhyay, S. Gallet, E. Franz, A. Persoons and T. Verbiest, *IEEE Trans. Magn.*, 2005, **41**, 4194–4196.
13 C. S. S. R. Kumar and F. Mohammad, *Adv. Drug Delivery Rev.*, 2011, **63**, 789–808.
14 S. U. Son, Y. Jang, J. Park, H. Bin Na, H. M. Park, H. J. Yun, J. Lee and T. Hyeon, *J. Am. Chem. Soc.*, 2004, **126**, 5026–5027.
15 C.-H. Jun, Y. J. Park, Y.-R. Yeon, J.-R. Choi, W.-R. Lee, S.-J. Ko and J. Cheon, *Chem. Commun.*, 2006, 1619–1621.
16 C. Altavilla and E. Ciliberto, *Inorganic Nanoparticles: Synthesis, Applications and Perspectives*, CRC Press, 1st edn, 2011.
17 L. S. Birks and H. Friedman, *J. Appl. Phys.*, 1946, **17**, 687.
18 B. D. Cullity, *Elements of X-ray Diffraction*, Prentice Hall, New Jersey, 2001.
19 C. Kumpf, R. B. Neder, F. Niederdraenk, P. Luczak, A. Stahl, M. Scheuermann, S. Joshi, S. K. Kulkarni, C. Barglik-Chory, C. Heske and E. Umbach, *J. Chem. Phys.*, 2005, **123**, 224707.
20 R. W. James, *The Optical Principles of the Diffraction of X-rays*, G. Bell and Sons Ltd, London, 1965.
21 P. G. Self, H. K. D. H. Bhadeshia and W. M. Stobbs, *Ultramicroscopy*, 1981, **6**, 29–40.
22 W. J. de Ruijter, R. Sharma, M. R. McCartney and D. J. Smith, *Ultramicroscopy*, 1995, **57**, 409–422.
23 S. Bals, B. Kabius, M. Haider, V. Radmilovic and C. Kisielowski, *Solid State Commun.*, 2004, **130**, 675–680.
24 M. M. Treacy, A. Howie and S. J. Pennycook, in *Inst. Phys. Conf. Ser. 52*, 1980, p. 261.
25 P. D. Nellist and S. J. Pennycook, *Adv. Imaging Electron Phys.*, 2008, **113**, 147–203.
26 D. H. Pearson, B. Fultz and C. C. Ahn, *Appl. Phys. Lett.*, 1988, **53**, 1405.
27 D. M. Pease, A. Fasihuddin, M. Daniel and J. I. Budnick, *Ultramicroscopy*, 2001, **88**, 1–16.
28 A. Falqui, V. Serin, L. Calmels, E. Snoeck, A. Corrias and G. Ennas, *J. Microsc.*, 2003, **210**, 80–88.
29 R. D. Leapman, L. A. Grunes and P. L. Fejes, *Phys. Rev. B: Condens. Matter Mater. Phys.*, 1982, **26**, 614–635.
30 L. Wang and Y. Yamauchi, *J. Am. Chem. Soc.*, 2010, **132**, 13636–13638.
31 C. T. Langlois, T. Oikawa, P. Bayle-Guillemaud and C. Ricolleau, *J. Nano Res.*, 2007, **10**, 997–1007.
32 W. Grogger, B. Schaffer, K. M. Krishnan and F. Hofer, *Ultramicroscopy*, 2003, **96**, 481–489.
33 S. Lozano-Perez, V. de Castro Bernal and R. J. Nicholls, *Ultramicroscopy*, 2009, **109**, 1217–1228.
34 M. A. Zalich, V. V. Baranauskas, J. S. Riffle, M. Saunders and T. G. St. Pierre, *Chem. Mater.*, 2006, **18**, 2648–2655.
35 S. Sun, C. Wang, S. Peng and L.-M. Lacroix, *Nano Res.*, 2009, **2**, 380–385.
36 H. T. Yang, C. M. Shen, Y. G. Wang, Y. K. Su, T. Z. Yang and H. J. Gao, *Nanotechnology*, 2004, **15**, 70–74.
37 S. Sun and C. B. Murray, *J. Appl. Phys.*, 1999, **85**, 4325.
38 L. T. M. Hoa, T. T. Dung, T. M. Danh, N. H. Duc and D. M. Chien, *J. Phys.: Conf. Ser.*, 2009, **187**, 012048.
39 H. Bönnemann and R. M. Richards, *Eur. J. Inorg. Chem.*, 2001, 2455–2480.
40 N. Yao and Z. L. Wang, *Handbook of Microscopy for Nanotechnology*, Kluwer Academic Publishers, 2005.
41 C. Colliex, T. Manoubi and C. Ortiz, *Phys. Rev. B: Condens. Matter Mater. Phys.*, 1991, **44**, 11402–11411.
42 Y. Zhao, T. E. Feltes, J. R. Regalbuto, R. J. Meyer and R. F. Klie, *J. Appl. Phys.*, 2010, **108**, 063704.